Journal of Magnetic Resonance 380 (2025) 107952

Contents lists available at ScienceDirect

Journal of Magnetic Resonance

journal homepage: www.elsevier.com/locate/jmr

# High-speed, high-memory NMR spectrometer and hyperpolarizer

Leo Joon Il Moon [a,b,1], William Beatrez [a,1], Jason Ball [c], Joan Mercade [c], Mark Elo [c], Angad Singh [a], Emanuel Druga [a], Ashok Ajoy [a,b,d,*]

[a] Department of Chemistry, University of California, Berkeley, Berkeley, CA 94720, USA
[b] Chemical Science Division, Lawrence Berkeley National Laboratory, Berkeley, CA 94720, USA
[c] Tabor Electronics Inc. Hatasia 9, Nesher, 3660301, Israel
[d] CIFAR Azrieli Global Scholars Program, 661 University Ave, Toronto, ON M5G 1M1, Canada

ARTICLE INFO

*Keywords:*
Arbitrary waveform transceiver
Dynamics nuclear polarization
Electron-nuclear spin control
Pulse sequence programming
Interpolation and decimation
Phase-sensitive detection
Quantum sensing

ABSTRACT

We report on the development of a novel nuclear magnetic resonance (NMR) spectrometer, incorporating a high-speed, commercially available arbitrary waveform transceiver (AWT) – Tabor Proteus P9484M. The spectrometer is optimized for integrated electron-nuclear spin control and dynamic nuclear polarization (DNP) and leverages the AWT's rapid sampling rate (9 Gs/s), significant memory capacity (16 GB), and efficient data transfer capabilities (6 Gs/s). These features enable effective NMR transmit–receive operations and electron control for DNP. In particular, the high sampling rates permit NMR pulse synthesis and signal reception directly at the Larmor frequency up to ~2.7 GHz. This can yield NMR signal-to-noise ratio (SNR) improvements by obviating the need for signal heterodyning. Additionally, the spectrometer features on-board, phase-sensitive detection, enabled by numerically controlled oscillators (NCO); and windowed acquisition can be carried out over extended periods and across millions of pulses, enabling the interrogation of nuclear spin dynamics directly in the rotating frame. The device's architecture opens up new avenues for NMR pulse control and DNP, including closed-loop feedback control, electron decoupling, 3D spin tracking, and potential applications in quantum sensing.

## 1. Introduction

Advances in nuclear magnetic resonance (NMR) spectroscopy and adjacent fields have historically often been spurred by innovations in instrumentation. Several transformative developments have emerged from such progress; to speak of a few: Fourier Transform (FT) techniques that enabled multidimensional NMR [1,2], strong gradients that have enabled single-shot NMR spectroscopy methods [3], integrated electron-nuclear spin control for dynamic nuclear polarization (DNP) [4–7], and infrastructure supporting non-traditional NMR pulse sequences that have resulted in numerous advancements [8–10].

However, as the science of NMR has matured and commercial NMR instruments have become widely accessible, they have been increasingly focused on traditional applications. There has, arguably, been a reduction in their hardware and software flexibility as a result. A greater need is being felt for customizable NMR instrumentation that can be adapted to a wide range of applications, including towards emerging methodology for DNP [11,12] and quantum sensing [13,14].

Motivated by this, in this paper, we introduce a new NMR spectrometer that leverages capabilities of modern arbitrary waveform transceivers (AWTs) [15]. The device is built around the Tabor Proteus P9484M [16] – a high-speed AWT with rapid sampling rates, large memory capacity, and fast data transfer capabilities (Section 2) – but is broadly compatible with other modern AWT devices. Ultimately, this integrates powerful capabilities for electron-nuclear control, NMR, and DNP in a compact, rack-mountable spectrometer.

We focus on the novel features of the device and resulting spectrometer. For inductive NMR acquisition, the AWT can *directly* receive signals at Larmor frequencies up to ~2.7 GHz, eliminating the need for signal heterodyning. This simplification can reduce the number of passive components and minimize insertion loss, facilitates effective digital filtering with minimal aliasing, and can yield gains in signal-to-noise ratios (SNR) (Section 4.4). The significant memory capacity (16 GB) and high-speed data transmission capabilities, and an onboard numerically controlled oscillator (NCO) [17] enable windowed data acquisition in a phase-sensitive manner over extended acquisition periods spanning millions of detection windows (Section 4.3).

On the transmission side, the device can directly synthesize arbitrarily shaped pulses in both the RF and microwave (MW) domains, at

* Corresponding author at: Department of Chemistry, University of California, Berkeley, Berkeley, CA 94720, USA.
*E-mail addresses:* jm2239@berkeley.edu (L.J.I. Moon), ashokaj@berkeley.edu (A. Ajoy).
[1] These authors contributed equally.

https://doi.org/10.1016/j.jmr.2025.107952
Received 31 May 2025; Received in revised form 5 August 2025; Accepted 8 August 2025
Available online 19 August 2025
1090-7807/© 2025 Published by Elsevier Inc.

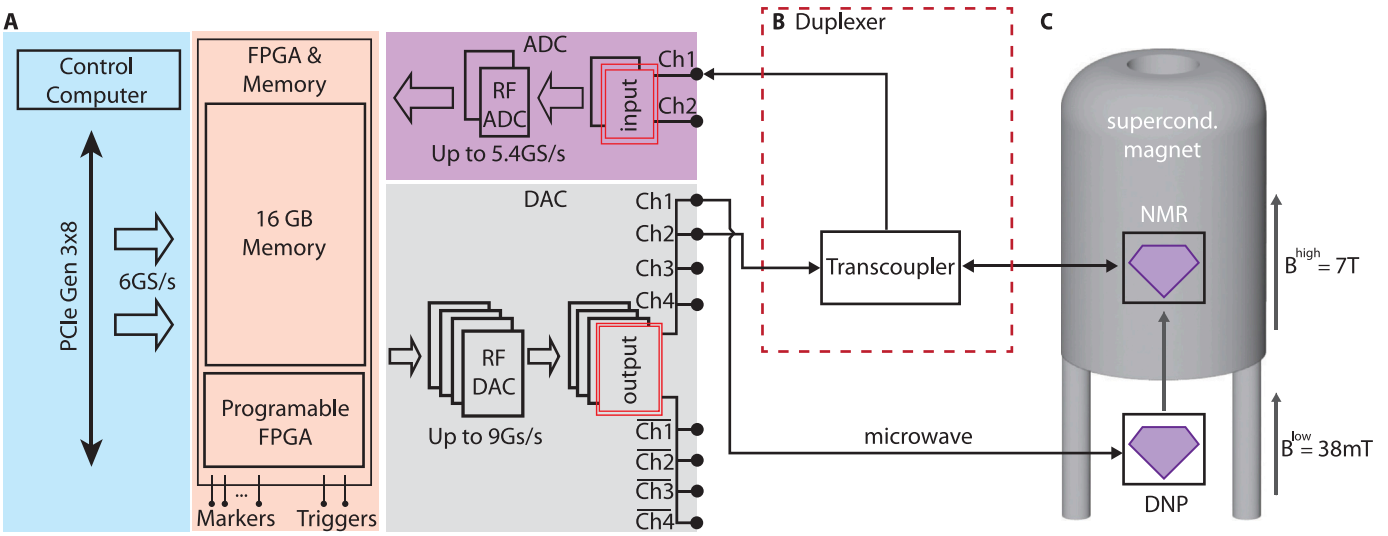


**Fig. 1.** Instrument schematic. Simplified block diagram of the Proteus AWT unit and NMR experimental setup. A, (Light Blue) The control computer connects to the Proteus P9484M via a high-speed PCIe Gen 3 × 8 interface, allowing communication speeds up to 6 Gs/s. (Orange) FPGA and Memory: The Proteus unit has 16 GB of memory, used for storing waveforms for the DAC and digitized signal from the ADC. The programmable FPGA configures the Proteus based on user commands. The marker system, with 2 markers per DAC channel, allows coherent control of external equipment, while the trigger ports enable external triggering of the Proteus. (Purple) ADC: The Proteus ADC has two channels. Channel 1 digitizes the analog signal from the NMR probe, relayed by duplexer at up to 5.4 Gs/s. The digitized data is processed by the FPGA and stored in memory. (Grey) DAC: The Proteus features 4 DAC channels and 4 corresponding inverted channels (180 degree off-phase from the non-inverted DAC channels) – marked as channels with over-lines – with a sampling rate of up to 9 Gs/s. The DAC generates analog signals using waveforms stored in the memory. An on-chip NCO can digitally up-convert these waveforms to produce analog signals at the desired frequency. B, Duplexer: The transcoupler relays the signal generated by the DAC to the NMR probe and sends the received signal to the ADC. Detailed transmit–receive circuit schematic is described in Fig. 2. C, Apparatus: The black box with a purple diamond indicates the $^{13}C$ nuclear spins inside a diamond. DNP from the nitrogen vacancy (NV) center to the $^{13}C$ nuclear spins occurs in low bias field ($B^{low}$ = 38 mT) for ~60 s (Section 3). The diamond sample is then moved to a high bias field generated by a superconducting magnet ($B^{high}$ = 7 T), where microwave pulses are applied to the hyperpolarized $^{13}C$ nuclear spins, and the signal is read out using NMR. Channel 1 of DAC is used to generate chirping microwave pulses for DNP (Fig. 7), and channel 2 of DAC is used to generate pulses to the $^{13}C$ nuclear spins. Channel 1 of ADC is used to readout the signal of the $^{13}C$ nuclear spins.

**Table 1**
**AWT Properties** We summarize the key features of the Proteus P9484M, as detailed in [16]. **DAC Properties,** The 4 channels of the DAC of the AWT offers a 9 Gs/s sampling rate, with 16 bit resolution in its amplitude. **Task Table Properties,** Each task table entry can be assigned a segment corresponding to a downloaded waveform. The task table can repeat an entry or a sequence of entries up to 1 million times, with a maximum of 64K entries and 32K sequences. This capability enables the generation of diverse pulse sequences without imposing significant memory or runtime constraints. **ADC Properties:** The AWT's ADC supports a sampling rate of up to 5.4 GHz, enabling signal reception up to 2.7 GHz with 12-bit vertical resolution.

| AWT Properties | | | |
|---|---|---|---|
| **DAC Properties** | | **Task Table Properties** | |
| Number of Channels | 4 | Max. task table length | 64K |
| Max. Sampling Rate | 9Gs/s | Max. task loops, Max. sequence loops | 1M |
| Amplitude | 1mV to 1.2Vpp | Max. subsequences | 32K |
| Resolution | 16 bits | Number of segments | ≤ 64k |
| **ADC Properties** | | | |
| Max. Sampling Rate | 5.4GHz/ 2.7GHz | Input Voltage Range | 0.5Vpp |
| Frequency Range | ≤ 2.7GHz | Resolution | 12 bits |

frequencies up to 13.5 GHz (at the third Nyquist zone). Customizable software, along with on-board digital oscillators and filters, further improves flexibility while simplifying hardware configurations. With a description of these capabilities towards integrated electron-nuclear spin control, we illustrate its potential to advance both traditional and emerging NMR applications.

## 2. AWT device architecture

The AWT device – central to the spectrometer construction here – integrates an arbitrary waveform generator (AWG) with a fast analog-to-digital converter (ADC) and high-capacity onboard memory. We note that AWTs have traditionally found use in radar and communication systems [18], and more recently for quantum computing hardware [19–23]; the same capabilities used in these applications are attractive in an NMR/DNP context.

As a representative example in this paper, we apply the spectrometer to experiments on a system of hyperpolarized $^{13}C$ nuclear spins in single-crystal diamond, which are polarized via optically pumped nitrogen-vacancy (NV) centers [24]. The AWT generates microwaves for low-field hyperpolarization and multi-pulse RF sequences for NMR interrogation of the nuclei at high field, and digitizes NMR signals. Ref. [25] describes the hyperpolarization apparatus and methodology; we instead focus here on the novel features of the AWT spectrometer towards these experiments (Fig. 1A).

Our implementation specifically uses the Tabor Proteus P9484M AWT (henceforth referred to as *"Proteus"*), but the concept can be replicated in similar systems. Fig. 1A shows a simplified block diagram [16], while Table 1 lists the device characteristics. The bottom of Fig. 2 shows a photograph of the device which is mounted a PXIe chassis.

We begin our discussion from the left side of Fig. 1A. Communication from the Proteus to the controlling computer occurs via Peripheral Component Interconnect Express (PCIe) Gen 3 × 8 (cyan region in Fig. 1A), enabling rapid data transfer rates up to 6 Gs/s [26]. Its on-board memory (orange block in Fig. 1A) supports data writing of up to 16 GB and is paired with a programmable Field-Programmable Gate Array (FPGA) [16].

For signal generation (gray region), the Proteus features four 9 Gs/s digital-to-analog converters (DACs), allowing signal output up to 9 GHz (second Nyquist zone). For a large class of NMR experiments, this potentially removes the need for external mixers and reduces

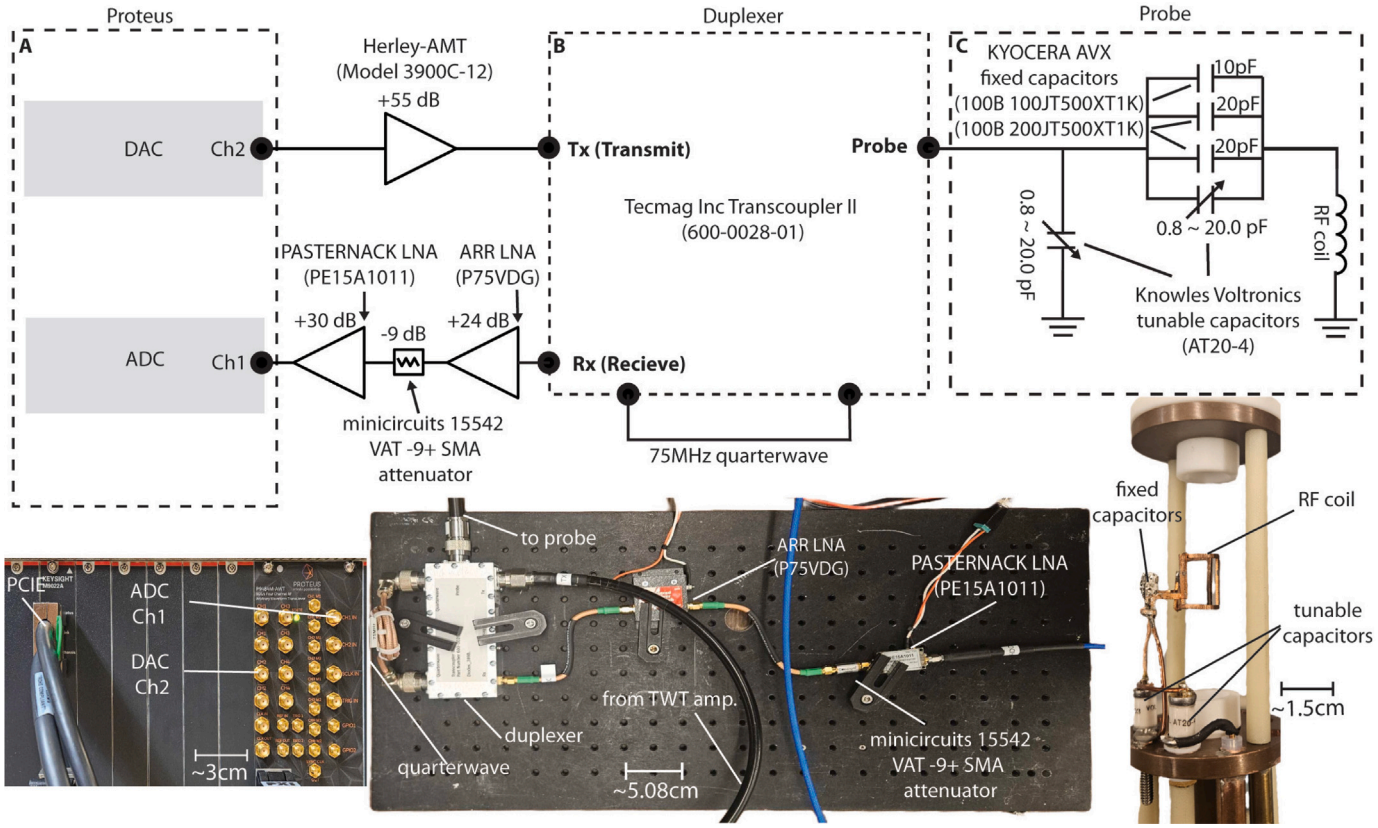


**Fig. 2.** Schematic of AWT based spectrometer implementation. A, Schematic of the AWT: Channel 2 of the DAC generates 75.38 MHz ($^{13}$C Larmor frequency at 7T) pulses, amplified by a TWT amplifier, and sent to the duplexer. Channel 1 of the ADC digitizes the$^{13}$C signal from the NMR probe, which is routed through the duplexer and amplified by two Low-Noise Amplifiers (LNAs) with a 9 dB attenuator in between. The 9 dB attenuator is inserted to reduce the intermodulation distortion between the two LNAs, and the each LNA is powered by a low-noise DC voltage and current source (Yokogawa GS 200). B, Schematic of the duplexer: The transmit (Tx) port receives 75.38 MHz pulses from Channel 2 of the DAC, amplified by a TWT amplifier. The probe port relays these pulses to the probe and also receives signals from the probe. A 75 MHz quarter-wave transformer matches the load impedance with the input impedance, minimizing reflected signals received from the probe. The receive (Rx) port relays the signal to two LNAs, with a 9 dB attenuator in between, for digitization by Channel 1 of the ADC. C, Schematic of the probe: Two tunable capacitors are used for matching and tuning. Three fixed capacitors set the RF coil's resonance frequency to 75.38 MHz, reducing the need to adjust the RF coil's inductance. Pictures and detailed part numbers for the components used in the setup are provided in the lower panels (see also Section 4).

the associated insertion losses. Built-in I/Q modulation is supported by two numerically controlled oscillators (NCOs) per channel, with waveforms stored in the 16 GB FPGA memory for digital up-conversion. A set of 8 Transistor–Transistor Logic (TTL) "markers" (2 per channel) allow deterministic triggering of external equipments allowing rapid control of amplifier blanking, field-cycling motion stages, lasers, and external AC-field sources (Section 6.2). The two trigger ports allows deterministic triggering of the output signal.

In the receive area (purple region, Fig. 1A), two inputs share a 5.4 Gs/s ADC, enabling one channel to operate at full rate or two channels at 2.7 Gs/s each. The captured NMR data is stored in the shared AWG memory. The large memory facilitates multiple windowed acquisitions per NMR measurement (Section 4.3). The raw data can be transmitted directly to a measurement PC for analysis; but additionally the FPGA provides signal-processing features, including interpolation, decimation, filtering, averaging, and potentially real-time decision-making and feed-forward capabilities (Section 4.1).

An important capability of the device is the digital down-conversion of raw data using the NCO as a reference, eliminating external down-conversion and ensuring coherent phase sensitive detection throughout the entire length of the measurement, including over multiple acquisition windows. This functionality underpins the ability to interrogate the nuclei *directly* in the rotating frame (Section 4.3). Triggers for data capture can be manual, external, or automated via AWT waveform playback. Command and control are streamlined through standard Virtual Instrument Software Architecture (VISA) protocols that are compatible with Python, MATLAB, and LabVIEW, ensuring seamless integration into existing workflows.

## 3. MW pulses for electron spin control

We first consider applications of the AWT for microwave generation in the context of low-field DNP, although a similar approach can be extended for applications in X-band EPR [27,28].

The maximum DAC sampling rate of 9 Gs/s facilitates direct MW generation up to 9 GHz, encompassing both the first (0–4.5 GHz) and second (4.5–9.0 GHz) Nyquist zones [29]. This approach can eliminate the need for external mixing infrastructure and reduce insertion losses. To reach higher frequencies, the third Nyquist zone (9–13.5 GHz) can also be utilized [30], though the output amplitude decreases according to the DAC's sinc-shaped frequency response $|\mathrm{sinc}(\pi f/f_s)|$, where $f$ is the frequency of interest, and $f_s$ is the sampling frequency. This attenuation affects all Nyquist zones and becomes more significant at higher frequencies. As an example of using the third Nyquist zone, a continuous-wave tone at 9.8 GHz can be generated by setting the NCO to 0.8 GHz and the sampling frequency to 9 GHz, utilizing the image frequency in the third Nyquist zone. Output power can be boosted using an accessory PXIe amplifier that spans from 100 kHz to 20 GHz (for e.g. [31]).

We apply the device to a low-field DNP sequence designed to transfer optically generated polarization of NV centers to bulk $^{13}$C nuclei in diamond, as detailed in Ref. [32,33]. This process involves a series of cascaded Landau–Zener anticrossings [34,35], achieved experimentally

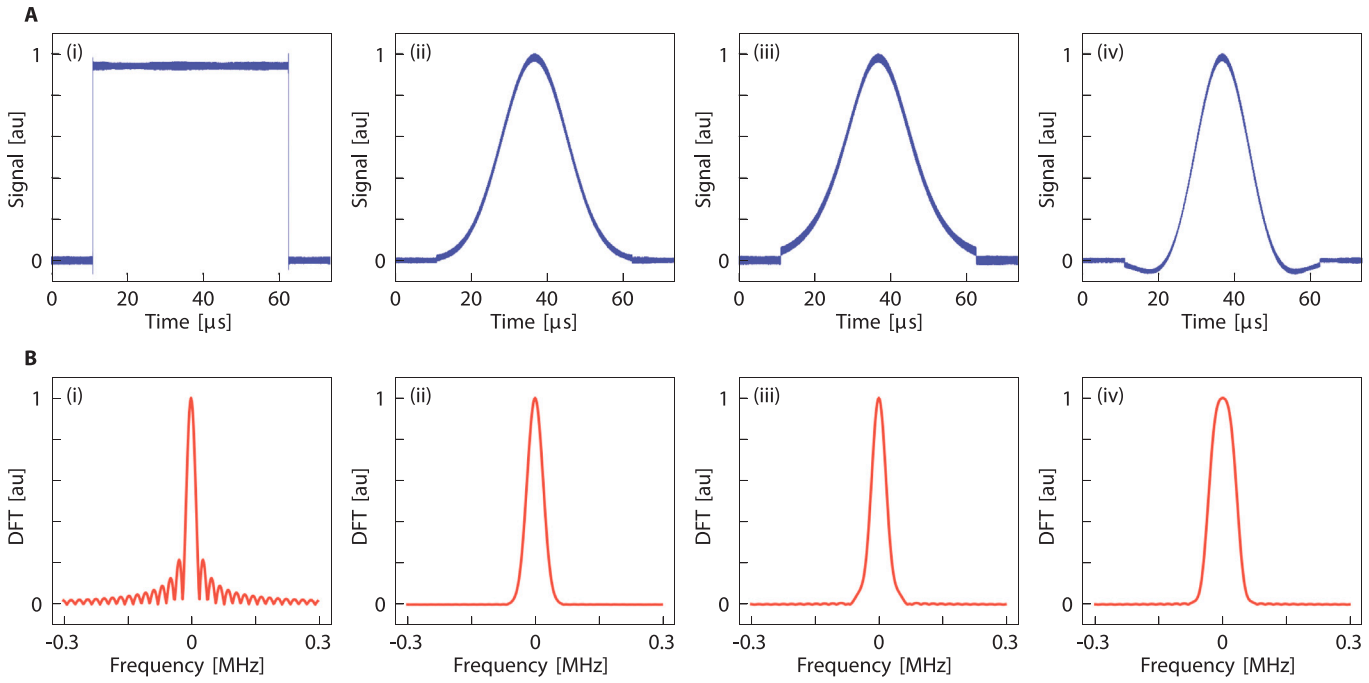


**Fig. 3.** Pulse shaping capabilities enabled by the AWT. A, Time-domain functions of the shaped pulses drawn by the AWT. Pulses are generated by the channel 2 of the AWT's DAC and digitized and digitally down-converted by the channel 1 of the AWT's ADC to obtain the pulse envelope. They consist of (i) rectangular, (ii) Gaussian, (iii) secant, and (iv) Hermite pulses. The generated pulse has a pulse duration of approximately 53 μs. B, Fourier transforms of the digital captures of the corresponding pulses.

through MW chirps across the NV center EPR spectrum at 38 mT, combined with continuous laser excitation [32,33,36]. To implement the MW chirps used in the DNP sequence, the chirped waveform with a linear frequency sweep from 3.404 GHz to 3.429 GHz at 750 sweeps per second is first downloaded to the AWT memory. The chirped waveform is then digitally up-converted to 3.779 GHz ± 12.5 MHz using an NCO set at 362.5 MHz [25,35]. They are subsequently amplified by a series of high-gain power amplifiers (Mini-Circuits ZVE-3W-83+ and ZHL-100W-382+), and applied simultaneously with 532 nm green laser excitation for ~60 s, depending on the $^{13}C$ $T_1$ times at the polarizing field, to yield hyperpolarization (see Fig. 1C). Both the NCO frequency and the waveform frequencies are adjustable but must be set appropriately to achieve the desired frequency sweep.

The *"task table"* feature of the AWT simplifies programming and supports memory efficiency. Multiple waveforms can be accommodated in memory and can be applied (or looped) in any order. Each waveform is assigned a segment number, allowing playback in any order, and can be repeated up to 1M times (with no cost to memory), skipped, or triggered externally. Table 1 presents the task table properties in more detail. Task entries contain instructions for playback, repetitions, and triggers, enabling seamless transitions between tasks and supporting complex pulse and DNP sequences. FPGA programming blocks further allow real-time decision-making, such as selecting waveforms based on ADC input levels.

In the simple DNP example above, a chirped waveform can be downloaded as a segment, and the task table can be programmed to repeat this segment up to the desired playback time without the need to rewrite the waveform. Additionally, the task table can accommodate more complex or customized sequences. In Ref. [37], we demonstrated the creation of different textures of nuclear polarization around the electron by applying alternating "sign" hyperpolarization sequences to the$^{13}C$ nuclei. This process involves using two chirped waveforms that sweep in opposite directions. By downloading these waveforms as segments once and assigning them in the task table, they can be played sequentially for desired playback time without the need for repeated waveform downloads.

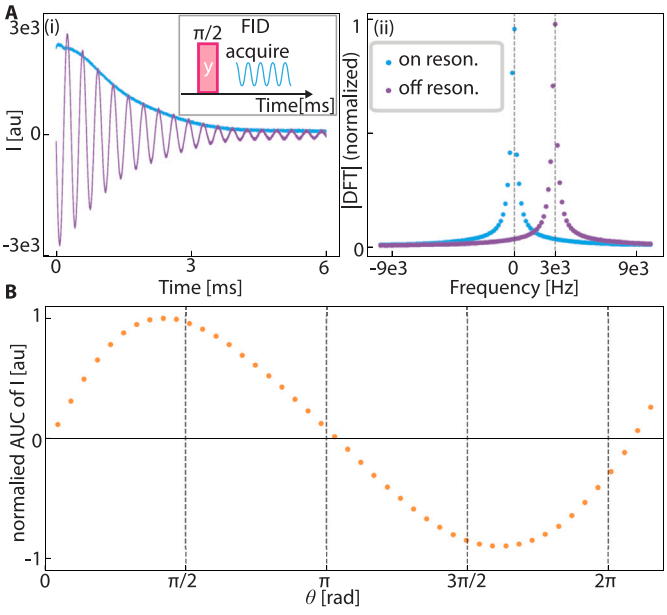


**Fig. 4.** FID and Rabi oscillations of hyperpolarized $^{13}C$ nuclei at 7T. A, (i) *Inset*: FID acquired for 6 ms, shown for on and off-resonance cases. The signal is measured by digitally down-converting using the NCO signal that is either on-resonant (light blue) or 3000 Hz off-resonant (purple). (ii) Fourier transform of the FID decay, after digital down-conversion with on/off-resonant NCO. B, Rabi oscillations obtained from FID by varying the angle ($\theta$) of the first $y$-pulse during FID acquisition and measuring the Area Under the Curve (AUC) of the In-phase (I) component. Normalization is done by setting the maximum AUC of I as 1. The nodes of the Rabi oscillations do not precisely align with $\pi/2$ and $3\pi/2$ due to two main factors: (1) RF inhomogeneity, and (2) the pulse ring-down, which is unaccounted for when we change the duration of the angle to set the angle $\theta$.

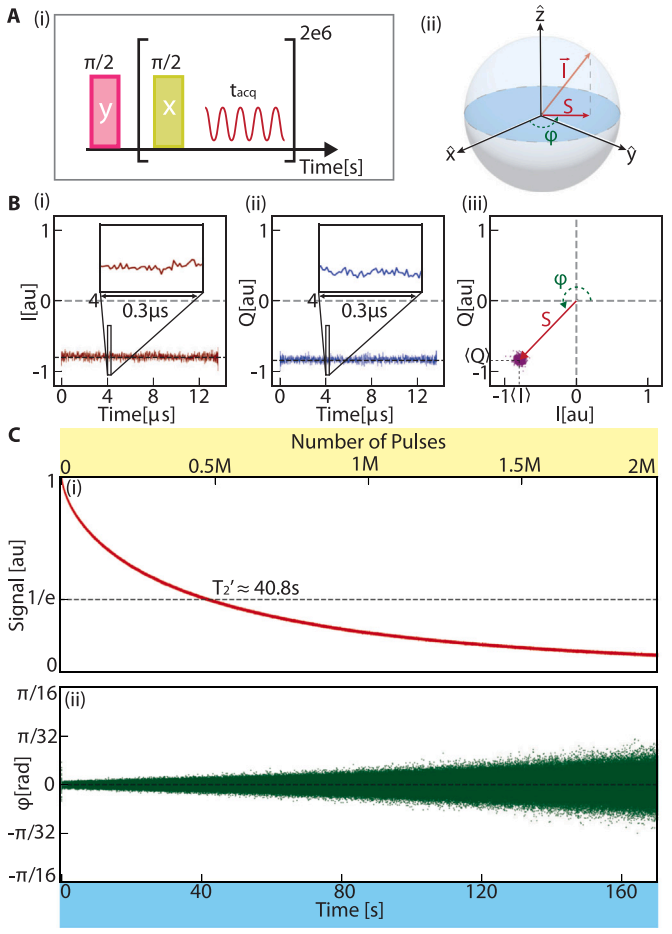


**Fig. 5.** Digital down-conversion for phase-sensitive detection. A, (i) Spin lock pulse sequence. After an initial $\pi/2$ $\hat{y}$-pulse, 2M $\pi/2$ $\hat{x}$-pulses are applied and the inductive $^{13}$C signal is obtained for $t_{acq}$ after every pulse. $t_{acq}$ is varied depending on the memory constraint, pulse spacing, and its position in the inter-pulse window is determined by the ring-down time of the probe. (ii) Bloch-sphere representation of the $^{13}$C nuclear spins. Depicted are the nuclear spins' magnetization ($\vec{I}$), its projection on its $\hat{x}-\hat{y}$ plane (S), and the phase ($\varphi$) of the $^{13}$C nuclear spins in the rotating frame. B, Using a home-built spectrometer, the signal amplitude and phase can be easily recovered. The NCO-assisted digitizer captures the (i) I and (ii) Q of the signal at each sampling point. Windows of $t_{acq} \approx 13.6$ μs of a signal capture for I and Q are shown, with insets showing a 0.3 μs zoom-in for clarity. (iii) Purple points show the I and Q values for one representative acquisition window. The red arrow represents the signal's amplitude (S), and the green angle ($\varphi$) indicates its phase. By averaging the purple data points collected in the I and Q plane, the norm and angle corresponding to S and $\varphi$ are determined. C, Tracking (i) the normalized signal and (ii) the phase of $^{13}$C nuclear spin over 160 s for each acquisition window. $t_{acq} \approx 4.6$ μs is used. Pulse sequence used is depicted in A(i), with pulse spacing $\tau \approx 36$ μs. $1/e$ time of the amplitude is $T_2' \approx 40.8$ s. There is a very slow overall drift in the phase (panel C(ii)) over long periods due to the pulse transients [38], but have removed this for simplicity.

## 4. AWT based NMR spectrometer

Transitioning from electron control applications, we now examine the capabilities of the AWT for RF control and readout of nuclear spins.

### 4.1. NMR pulse generation and capture: Interpolation and decimation

We first describe the generation of the NMR pulses. Fig. 2 shows a schematic of the transmit–receive RF circuit employed. Pictures of the assembled circuit are shown in the lower panel of Fig. 2B. Here, Ch.1 of the AWT's ADC is used for NMR receive, Ch.2 of the DAC for NMR transmit, and Ch.1 of the DAC is reserved for MW generation (see Section 3).

At the transmit end (Fig. 2A), RF pulses are digitally synthesized using techniques similar to chirped MW generation. Once generated by the AWT's DAC, these RF pulses are amplified with a 55 dBm Hurley traveling wave tube (TWT) amplifier and sent to the saddle coil in the probe (Fig. 2C) via a cross-diode duplexer (Fig. 2B). For $^{13}$C nuclei in a 300 MHz superconducting NMR magnet, the Larmor frequency (approximately 75 MHz) can be directly synthesized by the AWT's DAC. This approach contrasts with conventional NMR hardware, which typically requires additional mixing stages.

Fig. 3A illustrates representative examples of generated RF pulses, including (i) rectangular, (ii) Gaussian, (iii) secant, and (iv) Hermite pulse shapes. These pulse shapes are easy to generate as data arrays in Matlab or Python, making implementation straightforward. The data in Fig. 3A shows the produced pulses digitized by the same AWT. Fig. 3B shows the corresponding Fourier transform of these pulses, indicating a high degree of spectral purity.

We now provide specific details on pulse generation and data acquisition. The AWT employs two features to optimize memory utilization: (1) *interpolation* to reduce the memory required to store waveforms applied during transmission, and (2) *decimation* to decrease the readout memory window by downsampling at an integer factor during reception. Interpolation and decimation significantly reduces memory usage while preserving the essential characteristics of the pulse.

Pulse generation for the implementation in Fig. 3A begins by drawing a pulse envelope, represented by an array with 16-bit resolution. Each data point in the array corresponds to the envelope shape at intervals of $\frac{1}{675\times10^6}$ s, resulting in a sampling frequency of 675 MHz. This pulse envelope is then downloaded into the memory of the AWT.

When outputting the pulse, the AWT uses the downloaded pulse envelope and internally applies an 8x interpolation in hardware to increase the sampling rate to 5.4 GHz. Subsequently, it digitally mixes this interpolated signal with the AWT's on-chip NCO, which is set to the system's Larmor frequency. The advantage of this on-chip mixing is that it simplifies the pulse generation process, requiring only the drawing of the pulse envelope without needing to account for the pulse carrier frequency, hence also saving memory (as shown in Fig. 3A).

Finally, to capture the produced pulse shape, the AWT's output channel is directly connected to its ADC channel (purple region in Fig. 1A). The sampling rate of the AWT's ADC is set to 2.7 GHz. The AWT digitizes the pulse from its output while simultaneously digitally mixing it down using the receiver NCO, this is locked with pulse-generating NCO. This ensures accurate capture and demodulation to baseband with 12-bit vertical resolution (see Table 1). The AWT then saves the mixed-down pulse in its memory with a 16x decimation factor, resulting in data points being obtained every $\frac{16}{2.7\times10^9}$ s. Hardware constraints limit decimation to x1, x4, and x16, and interpolation to x1, x2, x4, and x8.

### 4.2. NMR receive circuit and standard experiments

The produced RF pulses following Fig. 3 are then delivered to the NMR probe as shown in Fig. 2. The homebuilt NMR probe is illustrated in the lower panel of Fig. 2C, and follows the design described in Ref. [39]. It features a saddle coil inductor (NMR coil) with tuning and 50-ohm impedance matching. The coil is fabricated from 1 mm thick oxygen-free high-conductivity (OFHC) copper via laser cutting. Design considerations, such as short capacitor leads and proper grounding to brass and copper ribs, ensure robust RF shielding.

We now focus our attention on the NMR receive circuit, shown in the lower panel of Fig. 2B. It is designed to detect weak nuclear induction signals generated on the same saddle coil [40]. These signals first pass through a 75 MHz quarter-wave line and a cross-diode duplexer (Tecmag 600-0028-01) (Fig. 2B). The duplexer ensures that only the intended signals pass through the transmit path, preventing the sensitive preamplifiers in the receive circuit from being exposed to the amplified pulses meant for the probe [40]. Subsequently, the

signal is amplified by a cascade of low-noise amplifiers — specifically the Advanced Receiver Research P75VDG and Pasternack PE15A1011 (Fig. 2A–B). For optimal performance, these amplifiers are powered by a low-noise DC voltage and current source (Yokogawa GS 200). Additionally, a 9 dB attenuator (Minicircuits 15542 VAT -9+ SMA attenuator) is inserted between the two amplifiers to reduce intermodulation distortion. The amplified signal is subsequently digitized through the decimation process described in Section 4.1, optimizing memory usage.

Fig. 4 shows the results of standard single-pulse experiments using the constructed spectrometer — an FID and Rabi oscillations of the hyperpolarized $^{13}$C nuclear spins at 7 T. Fig. 4A(i) presents single-shot time-domain FID data comparing cases where the NCO is either on-resonant or off-resonant, while Fig. 4A(ii) shows the corresponding Fourier transforms. Off-resonance excitation is applied by simply changing the AWT's NCO frequency. The FID decay time $T_2^* \approx 1.5$ ms, and corresponding spectrum linewidth 660 Hz is dominated by internuclear dipolar interactions [41].

Fig. 4B displays a typical $^{13}$C Rabi oscillation obtained by varying the length of the excitation pulse. Dashed lines are guides to the eye estimating the multiples of $\pi/2$ lengths. We ascribe the slightly non-sinusoidal behavior to two factors: (1) RF inhomogeneity across the diamond sample and (2) the pulse ring-down that is unaccounted for when we change the length of the pulse to change its angle $\theta$ [38].

### 4.3. Phase sensitive detection: multipulse windowed acquisition

A particularly attractive feature of the AWT is direct *phase-sensitive* digitization of the NMR signal at the Larmor frequency, leveraging the device's rapid sampling rate, and eliminating the need for down-mixing elements. Fig. 5 illustrates how this feature enables the extraction of both the phase and the amplitude of the NMR signal in a windowed acquisition for a representative multipulse sequence (Fig. 5A) consisting of a series of multiple spinlocking $\pi/2$ $\hat{x}$-pulses. The NMR signal is interrogated in $t_{acq}$ windows between the pulses.

Fig. 5B(i) and (ii) present real (I) and imaginary (Q) raw data acquired by the AWT for *one* representative $t_{acq} \approx 13.6$ μs signal window, sampled every approximately 5.9 ns (i.e. at a rate of 168.75 Ms/s from decimation). The sequence in Fig. 5A itself entails 2M such windows. In Fig. 5B(i–ii), the ≈ 75 MHz Larmor signal is digitally down-converted to DC by mixing with an in-phase and 90° off-phase NCO on-chip, set at the Larmor frequency (see Fig. 4A). Insets in Fig. 5B(i) and (ii) show a zoom in a 0.3 μs window. The high sampling of the data is evident. A Fourier transform of the signal exhibits a peak at or around zero-frequency, this represents the NMR signal.

Fig. 5B(iii) illustrates the IQ signals for the same window plotted simultaneously on a 2D plot. We can identify the radial position $S$ of the centroid (effectively the net signal amplitude), and its phase $\varphi$ as those of the net projection of the spin vector on the $\hat{x} - \hat{y}$ plane of the Bloch sphere *directly* in the rotating frame. This is shown schematically in Fig. 5A(ii). Indeed, therefore, AWT sampling at the Larmor frequency and digital mixing with a matched NCO provides a simple and effective way to translate the spin dynamics from the lab frame to the rotating frame. This capability is especially powerful when combined with the $S$ and $\varphi$ information from each acquisition window in the multi-pulse sequence in Fig. 5A. Since each acquisition window is referenced to the numerically controlled oscillator (NCO), the phase evolution during pulse periods is inherently accounted for, allowing precise discernment of $S$ and $\varphi$ directly in the rotating frame. In contrast, commercial hardware lacks this capability, resulting in phase signals with "ramps" due to unaccounted phase changes during pulse periods [42], which are exceedingly difficult to decode except in very specific cases.

To combine the multipulse data efficiently, the I and Q components of the raw data are averaged within each acquisition window. These average values, denoted henceforth as ⟨I⟩ and ⟨Q⟩, are marked in Fig. 5B(iii). The signal intensity and phase associated with each window are then directly extracted from these averages.

Fig. 5C presents the amplitude $S$ and phase $\varphi$ data from the spin-lock sequence in Fig. 5A(i) with 2M $\hat{x}$-pulses. We represent the phase after the first $\pi/2$ $\hat{x}$-pulse to be $\varphi = 0$. Fig. 5C(i) presents the corresponding amplitude signal $S$ over $t = 160$ s; this trace also contains 2M points. The dashed line denotes the $1/e$ decay time of $T_2' \approx 40.8$ s, significantly extended over the typical $T_2^*$ time [41] (see Fig. 4A). Fig. 5C(ii) displays the corresponding phase points, and reveals slight dephasing around $\varphi = 0$ at long times due to the decay of the spin-locked state. Combining this amplitude and phase data, together with a unitary constraint of the nuclear spin vector, can facilitate the quasi-continuous tracking of spins on a (half) Bloch sphere (Fig. 5A(ii)) [43].

### 4.4. Sensitivity comparisons

To benchmark the performance of the AWT-based spectrometer, its signal-to-noise ratio (SNR) was compared to that of a commercial Varian system (Agilent DD2 Spectrometer) under identical experimental conditions. This comparison involved systematically swapping individual components to assess their impact on SNR.

Fig. 6A illustrates the hyperpolarized pulsed spin-lock $^{13}$C signal, similar to Fig. 5C, measured using the AWT spectrometer which serves as a benchmark for the comparison. Inset Fig. 6A(i) shows the pulse sequence with pulse spacing $\tau = 43$ μs and $t_{acq} \approx 33.6$ μs, and a total of 563,064 pulses and acquisition windows for a total of 60 s. Fig. 6C(i)–(iii) displays the Fourier transform of the spin-lock decay signal acquired under three configurations, with corresponding schematics shown in Fig. 6B(i)–(iii). In these schematics, red boxes indicate home-built components as outlined in Fig. 2, while black boxes represent components from the commercial Varian system.

The first configuration (Fig. 6B(i)) utilized the Varian pulse sequencer and transmit/receive (T/R) circuit, but signal digitization was performed using the AWT spectrometer. In this setup, the Varian system heterodyned the signal output to 20 MHz. Due to limited memory capacity, the Varian system could not be used for full transmit and receive operations in this configuration.

The second configuration (Fig. 6B(ii)) replaced the Varian T/R circuit with a home-built T/R and preamplifier circuit (Fig. 2A–B) while maintaining the Varian pulse sequencer. Finally, the third configuration (Fig. 6B(iii)) employed the Proteus AWT pulse sequencer along with the home-built T/R and preamplifier circuit (Fig. 2). To ensure comparability, the transmit amplifier's input signal and the nuclear Rabi frequency is maintained identical across all configurations.

For each configuration, the measured signal was normalized to 1, and the noise was calculated by averaging 10,000 points from the wings of the log-scale power spectrum. The SNR values obtained are depicted in the gray numbers alongside the Fourier spectra in Fig. 6C. Using the Varian system (Fig. 6C(i)), an SNR of $2.9\times10^5$ was achieved.

Replacing the Varian duplexer and preamps (T/R circuit) with the home-built circuit modestly improved the SNR to $3.2\times10^5$, a ~1.1x increase, demonstrating that the simple home-built circuit performs comparably to the commercial counterpart (Fig. 6C(ii)). We note that information regarding the Varian duplexer or heterodyne circuit is proprietary and not available.

When the Varian pulse sequencer was substituted with the AWT (Fig. 6C(iii)), the SNR increased to $7.1\times10^5$, representing a 2.2x improvement over the configuration with the Varian pulse sequencer and a 2.4x improvement over the fully commercial system. While it is difficult to pinpoint the exact origin of this SNR improvement because of several proprietary parts in the Varian hardware, we attribute to the high spectral purity of the 75 MHz pulses generated by the AWT, and the lowering of component insertion losses due to direct synthesis and acquisition at the nuclear Larmor frequency.

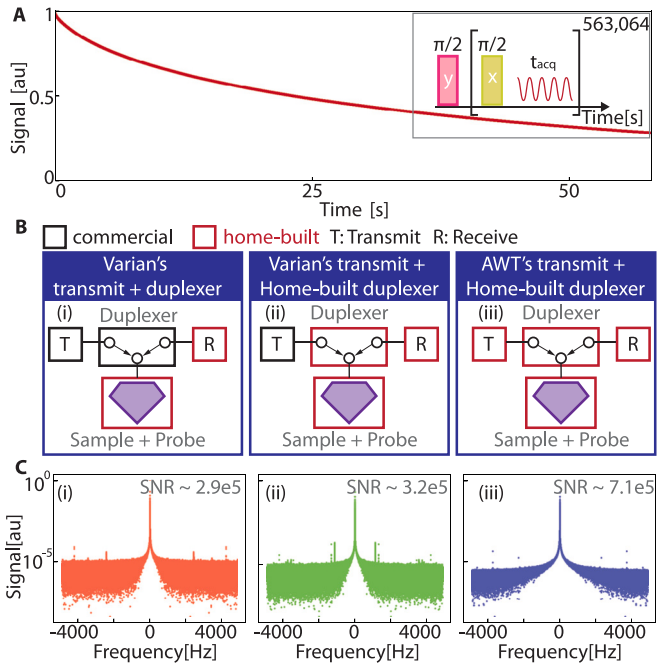


**Fig. 6.** Signal-to-noise comparison. To quantify the hardware performance of our home-built spectrometer relative to the commercial one, we measured representative $^{13}C$ pulsed spin-lock decay curves. A, Inset: Pulse sequence with spacing $\tau \approx 43$ μs and $t_{acq} \approx 33.6$ μs. A representative one-shot decay curve acquired using the home-built spectrometer is shown. Each data point (=563,064 total points) on this curve is obtained following Fig. 5B. B, Depiction of the transmit and receive configurations used for comparison: (i) using the commercial Varian for all aspects except signal digitization (done by the AWT); (ii) the Varian's transmit–receive circuit replaced with a home-built transmit–receive system (Fig. 2); and (iii) the fully home-built spectrometer, with pulses generated and digitized by the AWT. For clarity, red boxes indicate home-built components for measurements done in (i) to (iii), with "T" and "R" indicating transmit and receive, respectively. C,(i)-(iii) Fourier transforms of the spin-lock decay curves for the corresponding transmit and receive schemes, described in B(i) to (iii). The SNR values for all schemes are displayed in the respective plots. The spectrum generated using the AWT in conjunction with the home-built duplexer exhibits fewer unwanted spurs compared to the data produced by the Varian device.

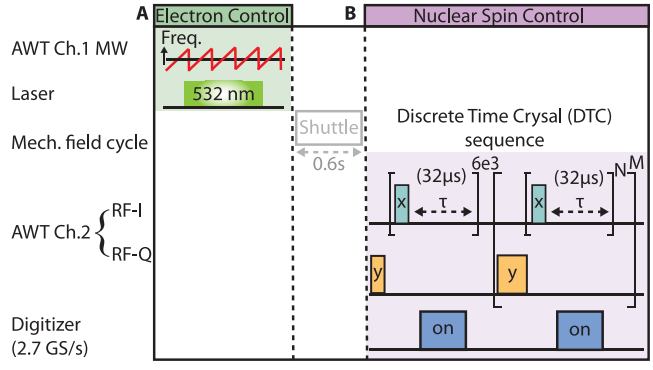


**Fig. 7.** Dual electron and nuclear spin control. Schematic of an experiment involving both hyperpolarization (electron spin control) and NMR (nuclear spin control). A, At low field ~38 mT, the diamond sample is irradiated with 10 ~1 W 532 nm lasers and microwave chirps [36]. B, After hyperpolarization, the sample is mechanically shuttled to high field ~7T, and the NMR control sequence is performed. Shown here is the DTC sequence. It begins with an initial $\pi/2$ $\hat{y}$-pulse, followed by a subsequent multiple-pulse spin-locking period to allow the transient spin signal to decay (~0.45 s). The modular DTC pulse sequence is then applied, consisting of a $\gamma_y$ (near $\pi$) $\hat{y}$-pulse inserted every N = 300 $\pi/2$ $\hat{x}$-pulses. M can be set up to 1M.

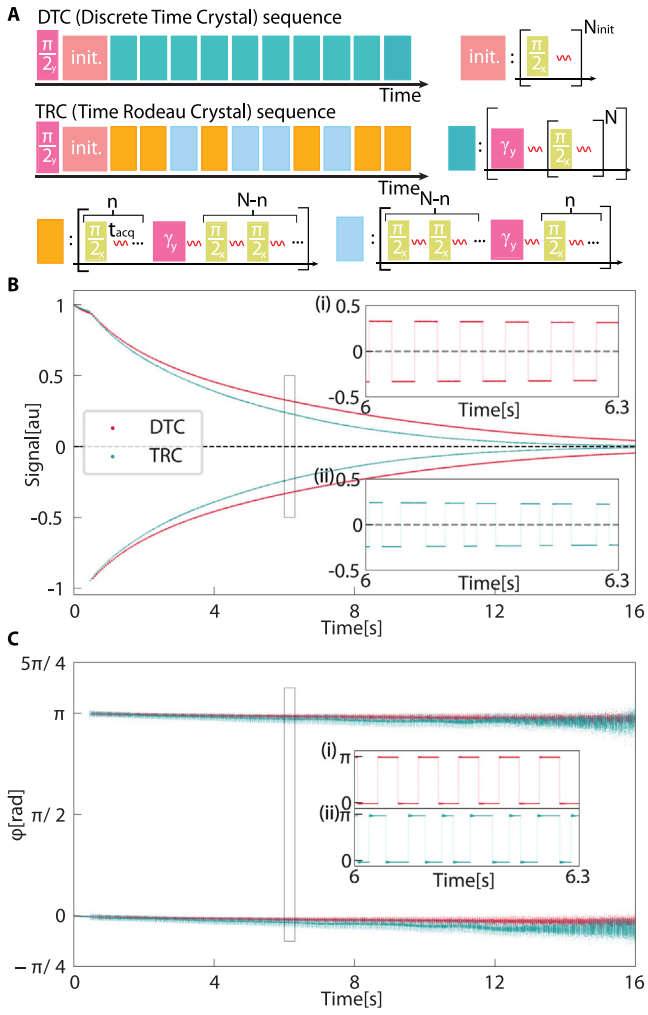


**Fig. 8.** DTC and Time Rondeau Crystal demonstration and utility of modular pulse sequences. A, Discrete Time Crystal (DTC) and Time Rondeau Crystal (TRC) sequences. $\gamma_y = \pi + \epsilon$, where $\epsilon$ is a small deviation from $\pi$. $N_{init} = 6000$, N = 300, n = 100, and $t_{acq} \approx 13.6$ μs. B, The expectation value of $I_x$ magnetization and C, the phase $\varphi$ in the $\hat{x} - \hat{y}$ plane are plotted against time. The first 6000 pulses represent the initial spin-lock along $+\hat{x}$ direction. Following this, the spins are flipped periodically (randomly) for the remainder of the curve, indicating the DTC (TRC) in red (dark green). The zoomed-in sections, marked with gray boxes, clearly show the periodic (random) switching of amplitude and phase within a 0.3s window of the larger curve for the DTC and the TRC.

## 5. Connections to previous work

We now present a comparison of the AWT spectrometer approach described here with previous literature. We note that the demand for greater flexibility in magnetic resonance (MR) instrumentation has been a recurring need in the community [44], and several pioneering devices based on arbitrary waveform generator (AWG) technology have been reported. Moreover, many groups have created home-built spectrometers using fast DAC/ADC cards, tailored for specific research needs [40]. However, while this work builds on these reports, the capability presented by the current AWT device is more comprehensive.

We especially highlight work from the Han group [28,45], which developed a home-built FPGA-based spectrometer suitable for both EPR applications. Takeda [46,47] and Mandal [48], Hilty [49] and their collaborators, presented a low-cost spectrometer utilizing on-chip components for NMR and NQR, while Tayler and co-workers recently demonstrated an Arduino-based ZULF spectrometer for zero-field NMR [50,51]. Jouda and his colleagues employed a lock-in amplifier for integrated waveform generation and detection in multinuclear NMR [52].

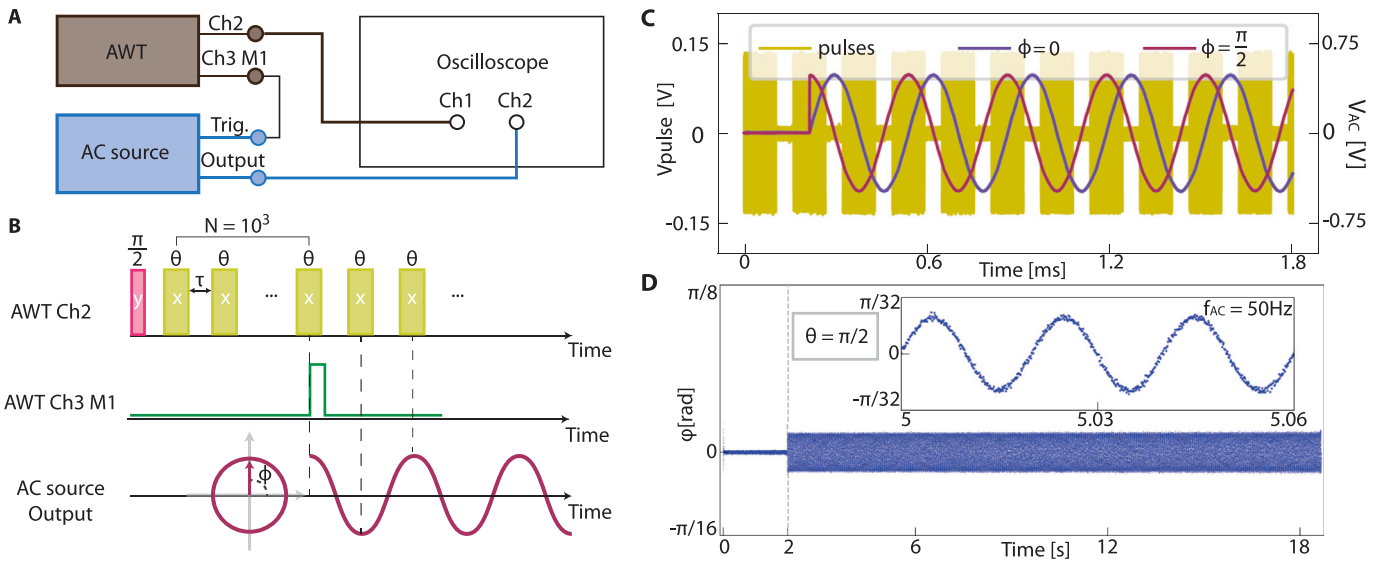


**Fig. 9.** Programmable TTL pulse generation and setting AC frequency synchronized with the pulse sequences. A, Depiction of the experimental setup used to obtain the data shown in C: Channel 2 of the AWT's DAC generates microwave pulses read by Channel 1 of the oscilloscope. Marker 1 of Channel 3 triggers the AC source (Tektronix 31000) in sync with the pulse sequence. The AC source output is connected to Channel 2 of the oscilloscope. B, Description of the AWT and AC source outputs: Channel 2 of the AWT's DAC generates the sequence with a train of $\theta$ $\hat{x}$-pulses, after an initial $\pi/2$ $\hat{y}$-pulse. Marker 1 of Channel 3 of the Proteus generates a 20 μs trigger at the midpoint of the 1000th $\theta$ $\hat{x}$-pulse. This trigger activates the AC source, which applies an AC field with phase 0 degrees (90 degrees), such that the nodes (anti-nodes) align with every $\theta$ $\hat{x}$-pulses. C, Oscilloscope traces: these traces show that the AC field with phase ($\phi$) 0 (blue) and 90 (dark red) are triggered in sync with the $\theta$ $\hat{x}$-pulses, with the AC field being triggered at the midpoint of the 1000th $\theta$ $\hat{x}$-pulse. D, Sensing AC field with spin-locking sequence: $\theta = \pi/2$ is used generate a spin-locking sequence for a sensing experiment with the $^{13}$C nuclear spins. An AC field with a frequency of 50 Hz, oscillating in the $\pm\hat{z}$ direction, is triggered precisely at the 2 s mark of the sequence. The AC field is imprinted on the phase $\varphi$ of the $^{13}$C nuclear spins, as shown in the inset, which zooms into the time window between 5 and 5.06 s. The slow drift in the phase has been removed, as done in Fig. 5C(ii).

Regarding commercial offerings, Spincore's PulseBlaster spectrometer and Tecmag systems have also provided increased flexibility compared to offerings from larger vendors.

Our current AWT spectrometer offers improved performance compared to previous efforts and even state-of-the-art commercial devices. It offers a faster sampling rate for both transmission and reception (see Table 1), significantly increased memory capacity, quicker communication, and enhanced modularity. These capabilities rival those of high-end commercial systems, yet the AWT spectrometer is available at a more competitive price.

## 6. Application to hyperpolarized NMR

We now describe the applications of AWT-based NMR spectroscopy for a few representative experiments.

### 6.1. Long-lived Discrete Time Crystals (DTCs)

One application is in experiments connecting magnetic resonance with new topics of interest to condensed matter physics. For example, we consider the construction of discrete time crystals (DTCs) with hyperpolarized $^{13}$C nuclear spins. DTCs exhibit a robust period-doubling response that is inherently resilient to pulse errors and disorder [53–55]. Unlike other demonstrations of DTC-like phenomena that rely on point-by-point measurements, the AWT allows for quasi-continuous signal acquisition (Fig. 5C) over extended durations without reinitialization [56]. This capability permits real-time observation of DTC formation and melting in a single shot, streamlining the experimental mapping of the DTC phase diagram [56,57]. While the physics of DTCs is detailed in Refs. [53–56], this discussion focuses on the AWT-enabled implementation.

In this case, the AWT is employed for hyperpolarization and nuclear spin control and readout, as shown in Fig. 7. During hyperpolarization (green block in Fig. 7), AWT's first channel (Ch.1) delivers chirped MW excitation (as described in Fig. 1) and 532 nm laser pumping at low magnetic fields for 60 s. The sample is then transferred to a 7T superconducting magnet, where Ch.2 generates NMR pulses applied to $^{13}$C nuclei, and the digitizer captures signals between pulses.

The DTC sequence is implemented through the task table, as displayed in Fig. 7B. Spins initialized to align along the $\hat{x}$-axis are tipped alternately between the $\hat{x}$ and -$\hat{x}$ axes using $\gamma_y$ $\hat{y}$-pulses, interspersed with N = 300 spin-locking pulses. The digitizer is activated in between the pulses, indicated as time window $\tau$ in Fig. 7. The DTC demonstrates robustness against imperfections in the $\gamma_y$ flip angle; a spin-flipping response is achieved even for deviations $\gamma_y = \pi \pm \epsilon$.

A generalized variant of the DTC pulse sequence was introduced recently by our group and collaborators referred to as *"time rondeau"* crystal [58]. The time rondeau crystal is a form of non-equilibrium order that exhibits both periodic oscillations and randomness in its order parameter ($I_x$ magnetization). When measured at stroboscopic times – corresponding to the first measurement window of the orange or light blue blocks in Fig. 8A – the order parameter oscillates periodically similar to those observed in discrete time crystals (DTCs). In contrast, measurements taken at half-integer times – corresponding to the midpoint of the orange or light blue blocks – the order parameter changes randomly [58]. As shown in Fig. 8A, it involves defining two distinct blocks: the first block consists of $(N - n)$ $\pi/2$ $\hat{x}$-pulses, one $\gamma_y$ $\hat{y}$-pulse, and $n$ $\hat{x}$-pulses, while the second block contains $n$ $\pi/2$ $\hat{x}$-pulses, one $\gamma_y$ $\hat{y}$-pulse, and $(N - n)$ $\hat{x}$-pulses. $N$ and $n$ are integers such that $0 < n < N/2$. After the initial 6000 $\pi/2$ $\hat{x}$-pulses, these two blocks are randomly arranged in any order. The AWT simplifies the implementation of these complex and/or randomized sequences.

Representative single-shot decay curves of the $I_x$ magnetization and the corresponding measured rotating frame phase (Section 4.3), $\varphi = \arctan(I_y/I_x)$, are illustrated in Fig. 8B-C for an exemplary case of $\gamma_y = 0.98\pi$, i.e. with imperfect pulses. In addition there is RF inhomogenity ever present in these experiments that contribute to pulse error (not quantified). Red and blue traces represent DTC and time rondeau crystal sequences, respectively. As shown in Fig. 8B, the spins consistently switch between +$\hat{x}$ and the -$\hat{x}$ axes despite the pulse error, achieving over 150 spin flips during the 16 s period. The inset in Fig. 8B offers a closer view of the experimental data, emphasizing a 0.3 s

window where the periodic (i) and random (ii) changes in the sign of $I_x$ are clearly visible.

The phase response, illustrated in Fig. 8C, exhibits periodic switching between rails that correspond to phase values of 0 ($\hat{x}$) and $\pi$ (-$\hat{x}$), respectively, with each $\gamma_y$-pulse. Insets (i) and (ii) provide a magnified view. The phase remains stable over hundreds of cycles, displaying minimal dephasing after $t$ = 16s. This stability highlights the AWT's capability to facilitate extended studies of dipolar-coupled systems [59, 60], utilizing its high sampling rate and memory capacity. We note that long and complex pulses sequences as Fig. 8A are very challenging to implement on commercial hardware.

### 6.2. Quantum sensing with hyperpolarized nuclei

In this example, we focus on the trigger capabilities of the instrument to synchronize external devices with the pulse sequence it produces. We apply it to a specific example of sensing of time-varying (AC) magnetic fields using hyperpolarized $^{13}$C nuclei. This experiment works on the principle that the nuclei when spin-locked, undergo secondary precessions in the rotating frame when exposed to an AC magnetic field; the precession carrying a direct imprint of the sensing field, and allowing its sensitive detection. For more details of the physics, we refer to [42,61].

For these experiments, we employ the AWT's capability to synchronize a function generator producing the AC magnetic field to be detected. As shown in Fig. 9A, the AWT generates pulses on Ch.2, while a trigger signal from Marker 1 of Ch. 3 synchronizes the AC field produced by a Tektronix 31000 function generator with the pulse sequence.

The pulse sequence for sensing, illustrated in Fig. 9B, involves a train of $\theta$ spin-locking pulses on the hyperpolarized $^{13}$C nuclei with pulse angle $\theta = \pi/2$. A marker was programmed to activate the AC field halfway through the 1000th $\hat{x}$-pulse. A 20 μs trigger (green) is utilized to switch on the AC field (red sine wave) on an edge trigger. The AC field itself is delivered along the $\hat{z}$ direction through a circular coil in the probe (Fig. 2C).

To illustrate the efficacy of the triggering capability, traces of the pulses and the synchronized AC field, captured using a Rigol DS7024 oscilloscope, are shown in Fig. 9C for clarity. It indicates the triggered AC field midway through the 1000th $\hat{x}$-pulse. The programmable pulse length and spacing provide precise adjustment of the AC field frequency and phase, allowing for alignment of its nodes (anti-nodes) at a 0° (90°) phase at the pulse midpoint. While this example uses a single trigger, the AWT can support up to ~30,000 synchronized triggers over extended durations.

Fig. 9D shows the resulting phase ($\varphi$) signal of the spin-locked hyperpolarized $^{13}$C nuclei analogous to Fig. 5C(ii), but when exposed to the AC field. Here $\theta = \pi/2$, $t_{acq} \approx 13.6$ μs, $\tau = 36$ μs and the signal is measured continuously for $t = 18$ s. The AC field is applied precisely at the 2 s mark. The phase signal serves as a direct imprint of the AC field; this is seen clearly in the 4 ms zoomed-in inset in Fig. 9D. Further details on the sensitivities achieved and comparison with other sensing methods can be found in Refs. [42,61]. In addition to sensing, this setup is capable of manipulating spins along specific 3D Bloch sphere trajectories while continuously monitoring them [43]. Overall, this example underscores the precision of the AWT in activating external devices and synchronizing pulse sequences with data acquisition blocks.

## 7. Outlook

The AWT-based spectrometer presented here leverages high-speed integrated ADC and DAC channels, large onboard memory, and fast communication capabilities (summarized in Fig. 1 and Table 1). These features enable fast sampling, phase-sensitive detection, and custom pulse sequences. At the very least, we envision that this device may enable retrofits of existing/legacy NMR infrastructure with enhanced capabilities with an attractive price point.

Looking ahead, however, the device holds promise for future applications. A particularly exciting avenue is implementing pulse sequences based on closed-loop feedback [62]. For example, in a spin-locking scheme, signals from one readout window could inform subsequent pulse decisions, allowing dynamic adjustments based on prior measurements. The relatively slow evolution of spin dynamics (tens of microseconds between pulses), combined with the AWT's fast decision-making capabilities, can facilitate on-the-fly feedback. For applications in long-term quantum sensing, such schemes could enhance spin control, improve stability against perturbations [63], and enable real-time correction of long-term noise processes [64].

Currently, data processing in Figs. 5B, 6 occurs offline on a PC, but we envision executing more complex computational tasks onboard the FPGA. This includes operations such as low-depth Fourier transforms and signal averaging, which, in the context of Figs. 5C and 6, could reduce memory requirements and allow for longer data collection durations. For instance, in a spin-locking scheme, onboard averaging of down-mixed signals could yield a single I/Q point per readout window. This would enable experiments lasting thousands of times longer than the current demonstration of a few million pulses. It could also enhance signal-to-noise ratios by capturing the entire nuclear induction signal between pulses.

The AWT's ability to control electrons at high frequencies also opens possibilities for advanced pulsed DNP and electron decoupling at high fields. Integrating electron and nuclear spin control within a single device could facilitate novel NMR-EPR measurements and pulsed DNP schemes at X-band frequencies or higher, advancing signal-enhanced spectroscopy and quantum sensing.

Finally, we recognize the importance of robust, user-friendly software to complement the hardware's flexibility. To this end, we are developing open-source packages in MATLAB and Python that enable the implementation of complex pulse sequences in a modular fashion, along with integrated signal acquisition. Additionally, we are working on integrating this software with existing platforms like OpenVnmrJ. We intend to make this available to the community and hope it will foster community-driven development and accessibility for advanced applications.

## CRediT authorship contribution statement

**Leo Joon Il Moon:** Writing – review & editing, Writing – original draft, Visualization, Validation, Supervision, Software, Resources, Project administration, Methodology, Investigation, Formal analysis, Data curation, Conceptualization. **William Beatrez:** Writing – original draft, Visualization, Validation, Supervision, Software, Resources, Project administration, Methodology, Investigation, Formal analysis, Data curation, Conceptualization. **Jason Ball:** Validation, Supervision, Software, Resources, Project administration, Methodology, Investigation, Formal analysis, Conceptualization. **Joan Mercade:** Validation, Supervision, Software, Methodology. **Mark Elo:** Validation, Supervision, Software, Resources, Project administration, Methodology, Investigation, Formal analysis, Conceptualization. **Angad Singh:** Writing – review & editing, Visualization. **Emanuel Druga:** Resources, Project administration, Methodology, Conceptualization. **Ashok Ajoy:** Writing – review & editing, Writing – original draft, Visualization, Validation, Supervision, Software, Resources, Project administration, Methodology, Investigation, Funding acquisition, Conceptualization.

## Declaration of competing interest

The authors declare the following financial interests/personal relationships which may be considered as potential competing interests: Ashok Ajoy, William Beatrez, Joon Il Moon has patent HIGH-SPEED,

HIGH-MEMORY NMR SPECTROMETER AND HYPERPOLARIZER pending to THE REGENTS OF THE UNIVERSITY OF CALIFORNIA. If there are other authors, they declare that they have no known competing financial interests or personal relationships that could have appeared to influence the work reported in this paper.


## Acknowledgments

This work was funded by NSF MRI, United States (2320520), AFOSR, United States DURIP (FA9550-22-1-0156), ONR, United States (N00014-20-1-2806), DOE SBIR, United States (72521), and the CIFAR Azrieli Foundation, Canada (GS23-013).


## Appendix A. Component list

To aid clarity, Table A.2 summarizes the key components required to construct the spectrometer depicted in Fig. 2.

## Appendix B. Spectral purity

To evaluate the spectral purity of the pulses used for nuclear spin control with the constructed spectrometer, we investigated potential spurious signals arising from the digital-to-analog conversion stage within the AWT. In this analysis, we focus specifically on the output of the Proteus DAC, deliberately excluding contributions from the Herley-AMT high-power amplifier to isolate the effects of the AWT itself.

Indeed, one of the major source of spurious signals in AWGs is quantization noise, which arises from the finite resolution of the DAC when converting continuous waveforms into discrete digital values. In conventional AWG configurations, when a periodic waveform (e.g., a carrier) has an integer number of samples per cycle, the quantization error can repeat deterministically. This periodicity results in spurs at harmonic frequencies, that typically degrades spectral purity.

To mitigate this effect, the Proteus AWG employs a Digital Up-Conversion (DUC) architecture in which the carrier frequency is generated in real-time using a high-resolution phase accumulator (48 bits). This approach ensures that the carrier is not perfectly aligned with the sampling grid, thereby preventing cyclic repetition of quantization error. As a result, the quantization noise becomes decorrelated from the waveform and is spread uniformly across the output bandwidth, rather than concentrating into discrete spurious tones. This significantly enhances the spurious-free dynamic range (SFDR) of the output signal.

Fig. B.10 shows the measured spectrum of a single-tone 75.38 MHz signal generated directly from the Proteus DAC. This frequency serves as the central tone for pulses applied to $^{13}C$ spins at 7T. The measurement spans 600 kHz around the tone center. The spectrum demonstrates excellent spectral purity, with an observed SFDR of 107.9 dB.

This analysis confirms that the DAC output of the Proteus AWT, when used in DUC mode, offers high spectral purity suitable for precision spin control applications in NMR and DNP experiments.

## Appendix C. NCO specification and phase coherence

We provide here the specifications of the NCOs used in both the AWG (DAC) and digitizer (ADC) sections of the Proteus arbitrary waveform transceiver (AWT), as well as a description of how phase coherence is maintained between them.

The DAC-side NCO (AWG section) supports a frequency range from DC to 9 GHz, with a frequency resolution of 32μ Hz when operating at a 9 GS/s sampling rate. The ADC-side NCO (digitizer section) supports a frequency range up to 2.7 GHz, with a frequency resolution of 0.63 Hz at a 2.7 GS/s sampling rate.

Maintaining phase coherence between the DAC and ADC NCOs is essential for phase sensitive detection. To achieve this, the Proteus AWT architecture ensures that both the AWG and digitizer sections share a common reference clock. The DAC typically operates at a sampling rate $N$ times higher than the ADC, using a frequency divider (denoted as :N in Fig. C.11B) to maintain clock synchronization across both domains (see Fig. C.11B).

Despite the DAC and ADC having different clock rates and differing bit lengths for internal registers (e.g. phase accumulator), the Proteus firmware internally computes appropriate phase increments for each domain such that the phase increment per second remains strictly identical for both domains. This ensures that the NCOs remain phase-locked, preserving coherence in frequency and phase throughout the acquisition window.

For example, a DAC sample rate of 9 GS/s and an ADC sample rate of 2.25 GS/s (i.e., N = 4) will maintain exact phase synchronization, allowing the same numerically generated carrier to be used for both upconversion and downconversion without introducing phase drift.

Fig. C.11 illustrates this mechanism in a simplified block diagram, showing the matched phase accumulators and shared reference architecture. Further explanation is included in the figure caption.

**Table A.2**
**Components** to build the spectrometer shown in Fig. 2.

| Component List | |
|---|---|
| AWT | Proteus P9484M (Tabor Electronics) |
| NMR amplifier | Herley AMT, 3900C-12 (Herley) |
| duplexer | Transcoupler II 600-0028-01 (Tecmag) |
| amplifier | PE15A1011 Low-Noise Amplifier (Pasternack) |
| attenuator | 15542 VAT -9+ SMA Attenuator (Minicircuits) |
| pre-amplifier | P75VDG Low-Noise Amplifier (Advanced Receiver Research) |
| quarter-wave impedance transformer | RG142 Coax UHF male to UHF male 75MHz Quarterwave (Pasternack) |
| DC Voltage source | GS 200 DC Voltage / Current Source (Yokogawa) need x2 |

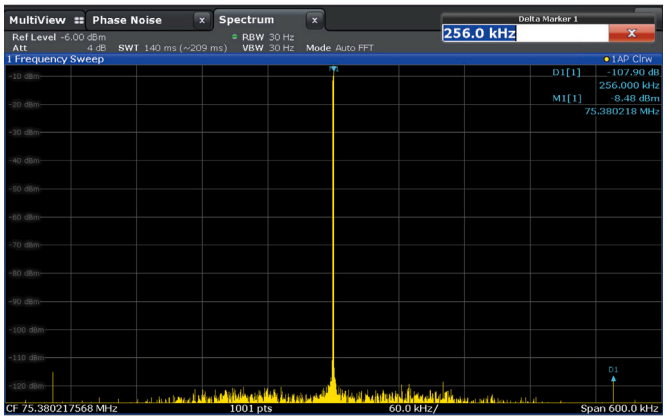


**Fig. B.10.** Spectrum analyzer output showing measurement of the Proteus DAC. The $x$-axis represents frequency and the $y$-axis represents power in dBm. Output is shown for a continuous-wave single-tone at 75.38 MHz. Spectrum analyzer was configured with a center frequency of 75.38 MHz and a span of 600 kHz. Delta marker (D1) in the top-right corner indicates the power ratio between the main tone and the largest spurious signal, measured to be 107.9 dB. This value corresponds to the spurious-free dynamic range (SFDR) of the DAC output.

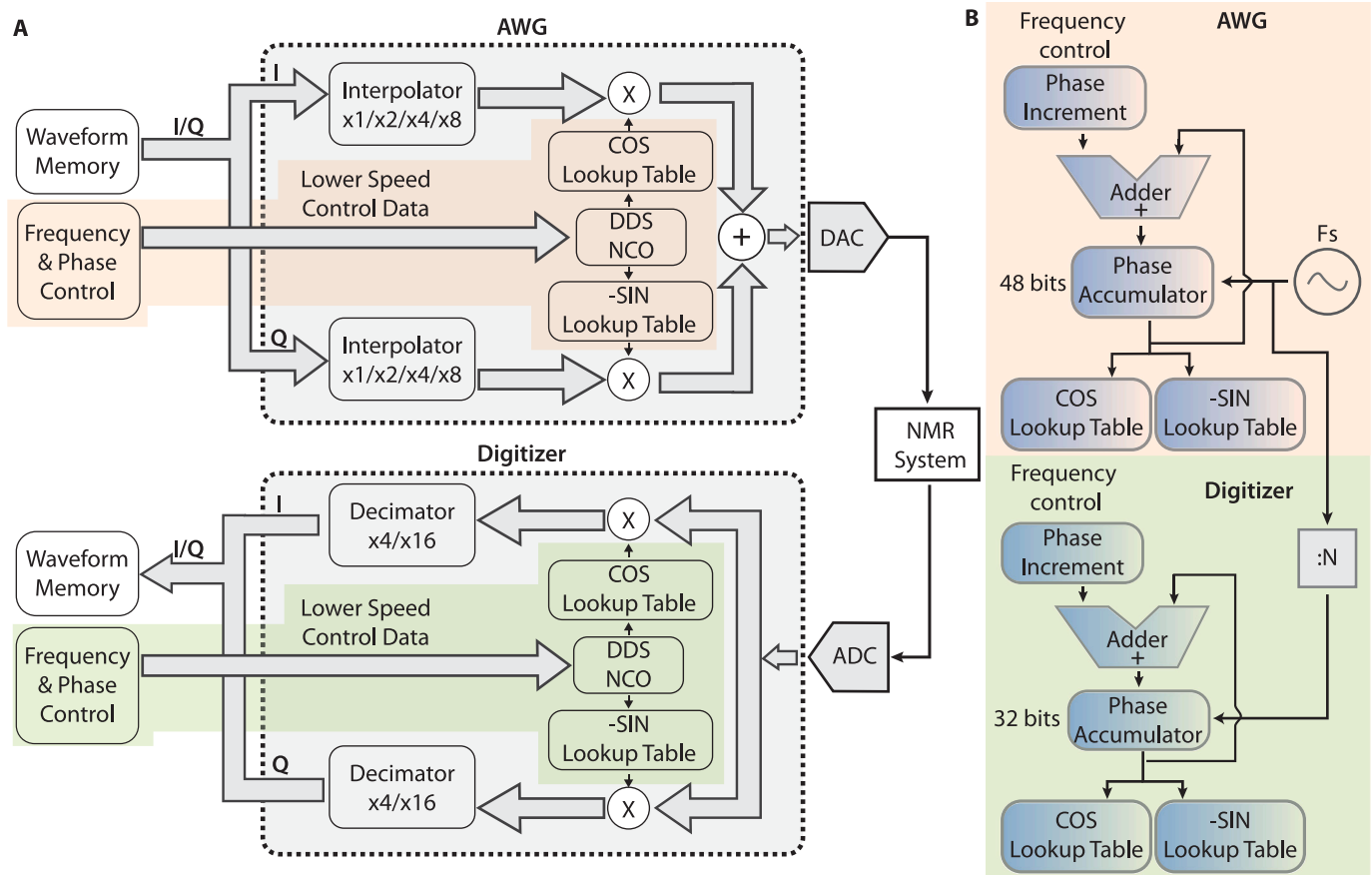


**Fig. C.11.** Block diagram illustrating the interaction between the NCO, DAC, and ADC. A, *Block diagram of the AWG section.* I (in-phase) and Q (quadrature) components are loaded from waveform memory, pass through an interpolator to reconstruct under-sampled waveforms, and are mixed with a DDS (Direct Digital Synthesis)-generated NCO using cosine and -sine lookup tables. The resulting signals are summed and sent to the DAC, which drives the NMR system. *Block diagram of the Digitizer section.* The structure mirrors the AWG but in reverse: signals from the NMR system are digitized by the ADC, down-sampled via a decimator, and stored in waveform memory. Light orange (green) regions indicate where the NCO's frequency and phase are controlled in the AWG (Digitizer). Lower-speed control data sets the DAC and ADC sampling rates for waveform generation or acquisition. B, Light orange (green) regions show how the NCO is generated in the AWG (Digitizer) section. The frequency control block sets the phase increment value, calculated by the Proteus firmware to ensure phase coherence. The phase accumulator integrates this increment each clock cycle, feeding the resulting phase into cosine and sine lookup tables to produce the I/Q waveforms. The phase accumulator loops back into the adder to continuously update the phase over time. The Digitizer follows a similar architecture but employs a shorter accumulator bit length. Here, Fs denotes the sampling rate of the respective clock. Despite differences in both bit width and sampling rate, set by a : N frequency divider between the DAC and ADC, the firmware computes appropriate phase increment values to ensure that the phase advancement per second remains strictly identical between the AWG and Digitizer.

## Data availability

Data will be made available on request.

## References


[1] R.R. Ernst, Nuclear magnetic resonance Fourier transform spectroscopy (Nobel lecture), Angew. Chem. Int. Ed. Engl. 31 (7) (1992) 805–823.

[2] R.R. Ernst, G. Bodenhausen, A. Wokaun, Principles of Nuclear Magnetic Resonance in One and Two Dimensions, Oxford University Press, 1990.

[3] L. Frydman, A. Lupulescu, T. Scherf, Principles and features of single-scan two-dimensional NMR spectroscopy, J. Am. Chem. Soc. 125 (30) (2003) 9204–9217.

[4] T. Maly, G.T. Debelouchina, V.S. Bajaj, K.-N. Hu, C.-G. Joo, M.L. Mak-Jurkauskas, J.R. Sirigiri, P.C. Van Der Wel, J. Herzfeld, R.J. Temkin, et al., Dynamic nuclear polarization at high magnetic fields, J. Chem. Phys. 128 (5) (2008).

[5] A.C. Torrezan, M.A. Shapiro, J.R. Sirigiri, R.J. Temkin, R.G. Griffin, Operation of a continuously frequency-tunable second-harmonic CW 330-GHz gyrotron for dynamic nuclear polarization, IEEE Trans. Electron Devices 58 (8) (2011) 2777–2783.

[6] K.O. Tan, C. Yang, R.T. Weber, G. Mathies, R.G. Griffin, Time-optimized pulsed dynamic nuclear polarization, Sci. Adv. 5 (1) (2019) eaav6909.

[7] J. Eills, D. Budker, S. Cavagnero, E.Y. Chekmenev, S.J. Elliott, S. Jannin, A. Lesage, J. Matysik, T. Meersmann, T. Prisner, et al., Spin hyperpolarization in modern magnetic resonance, Chem. Rev. 123 (4) (2023) 1417–1551.

[8] C.A. Barnes, A.J. Robertson, J.M. Louis, P. Anfinrud, A. Bax, Observation of $\beta$-amyloid peptide oligomerization by pressure-jump NMR spectroscopy, J. Am. Chem. Soc. 141 (35) (2019) 13762–13766.

[9] M. Schledorn, A.A. Malär, A. Torosyan, S. Penzel, D. Klose, A. Oss, M.-L. Org, S. Wang, L. Lecoq, R. Cadalbert, et al., Protein NMR spectroscopy at 150 kHz magic-angle spinning continues to improve resolution and mass sensitivity, ChemBioChem 21 (17) (2020) 2540–2548.

[10] S. Xu, V.V. Yashchuk, M.H. Donaldson, S.M. Rochester, D. Budker, A. Pines, Magnetic resonance imaging with an optical atomic magnetometer, Proc. Natl. Acad. Sci. 103 (34) (2006) 12668–12671.

[11] K.O. Tan, S. Jawla, R.J. Temkin, R.G. Griffin, Pulsed dynamic nuclear polarization, in: Handbook of High Field Dynamic Nuclear Polarization, Hoboken, NJ, USA, 2020, pp. 71–86.

[12] M. Levien, L. Yang, A. van der Ham, M. Reinhard, M. John, A. Purea, J. Ganz, T. Marquardsen, I. Tkach, T. Orlando, et al., Overhauser enhanced liquid state nuclear magnetic resonance spectroscopy in one and two dimensions, Nat. Commun. 15 (1) (2024) 5904.

[13] C.L. Degen, F. Reinhard, P. Cappellaro, Quantum sensing, Rev. Modern Phys. 89 (3) (2017) 035002.

[14] N. Aslam, M. Pfender, P. Neumann, R. Reuter, A. Zappe, F. Fávaro de Oliveira, A. Denisenko, H. Sumiya, S. Onoda, J. Isoya, et al., Nanoscale nuclear magnetic resonance with chemical resolution, Sci. 357 (6346) (2017) 67–71.

[15] Q. Gu, RF System Design of Transceivers for Wireless Communications, Springer Science & Business Media, 2006.

[16] Tabor Electronics, Proteus series datasheet, 2024, Ver. 3.33.

[17] S. Kadam, D. Sasidaran, A. Awawdeh, L. Johnson, M. Soderstrand, Comparison of various numerically controlled oscillators, in: The 2002 45th Midwest Symposium on Circuits and Systems, 2002, MWSCAS-2002, Vol. 3, IEEE, 2002, III–III.

[18] A.J. Fenn, D.H. Temme, W.P. Delaney, W.E. Courtney, The development of phased-array radar technology, Linc. Lab. J. 12 (2) (2000) 321–340.

[19] M.T. Baig, M. Johanning, A. Wiese, S. Heidbrink, M. Ziolkowski, C. Wunderlich, A scalable, fast, and multichannel arbitrary waveform generator, Rev. Sci. Instrum. 84 (12) (2013).

[20] R. Bowler, U. Warring, J.W. Britton, B. Sawyer, J. Amini, Arbitrary waveform generator for quantum information processing with trapped ions, Rev. Sci. Instrum. 84 (3) (2013).

[21] Y. Xu, G. Huang, J. Balewski, R. Naik, A. Morvan, B. Mitchell, K. Nowrouzi, D.I. Santiago, I. Siddiqi, Qubic: An open-source FPGA-based control and measurement system for superconducting quantum information processors, IEEE Trans. Quantum Eng. 2 (2021) 1–11.

[22] J. van der Heijden, F. Berritta, T. Rasmussen, F. Ansaloni, F. Fedele, S. Fallahi, G. Gardner, M. Manfra, Y. Cohen, J. Kutchinsky, et al., Universal qubit control through FPGA-accelerated qubit classification, Hamiltonian estimation and real-time feedback [Part 1], in: APS March Meeting Abstracts, Vol. 2023, 2023, pp. M74–007.

[23] G.Q. AI, et al., Quantum error correction below the surface code threshold, Nat. 638 (8052) (2024) 920.

[24] R. Fischer, C.O. Bretschneider, P. London, D. Budker, D. Gershoni, L. Frydman, Bulk nuclear polarization enhanced at room temperature by optical pumping, Phys. Rev. Lett. 111 (5) (2013) 057601.

[25] A. Ajoy, R. Nazaryan, E. Druga, K. Liu, A. Aguilar, B. Han, M. Gierth, J.T. Oon, B. Safvati, R. Tsang, et al., Room temperature "optical nanodiamond hyperpolarizer": Physics, design, and operation, Rev. Sci. Instrum. 91 (2) (2020).

[26] T. Fountain, A. McCarthy, F. Peng, et al., PCI express: An overview of PCI express, cabled PCI express and PXI express, in: 10th ICALEPCS Int. Conf. on Accelerator and Large Expt. Physics Control Systems, 2005.

[27] J.E. McPeak, R.W. Quine, S.S. Eaton, G.R. Eaton, An x-band continuous wave saturation recovery electron paramagnetic resonance spectrometer based on an arbitrary waveform generator, Rev. Sci. Instrum. 90 (2) (2019).

[28] T. Kaufmann, T.J. Keller, J.M. Franck, R.P. Barnes, S.J. Glaser, J.M. Martinis, S. Han, DAC-board based X-band EPR spectrometer with arbitrary waveform control, J. Magn. Reson. 235 (2013) 95–108.

[29] W. Kester, What the Nyquist criterion means to your sampled data system design, Analog. Devices (2009) 1–12.

[30] W.D. Kalfus, D.F. Lee, G.J. Ribeill, S.D. Fallek, A. Wagner, B. Donovan, D. Ristè, T.A. Ohki, High-fidelity control of superconducting qubits using direct microwave synthesis in higher Nyquist zones, IEEE Trans. Quantum Eng. 1 (2020) 1–12.

[31] Tabor Electronics, TE3201-2 datasheet ver. 1.4, 2024, Ver. 1.4.

[32] A. Ajoy, K. Liu, R. Nazaryan, X. Lv, P.R. Zangara, B. Safvati, G. Wang, D. Arnold, G. Li, A. Lin, et al., Orientation-independent room temperature optical 13C hyperpolarization in powdered diamond, Sci. Adv. 4 (5) (2018) eaar5492.

[33] A. Ajoy, R. Nazaryan, K. Liu, X. Lv, B. Safvati, G. Wang, E. Druga, J. Reimer, D. Suter, C. Ramanathan, et al., Enhanced dynamic nuclear polarization via swept microwave frequency combs, Proc. Natl. Acad. Sci. 115 (42) (2018) 10576–10581.

[34] P.R. Zangara, S. Dhomkar, A. Ajoy, K. Liu, R. Nazaryan, D. Pagliero, D. Suter, J.A. Reimer, A. Pines, C.A. Meriles, Dynamics of frequency-swept nuclear spin optical pumping in powdered diamond at low magnetic fields, Proc. Natl. Acad. Sci. 116 (7) (2019) 2512–2520.

[35] A. Pillai, M. Elanchezhian, T. Virtanen, S. Conti, A. Ajoy, Electron-to-nuclear spectral mapping via dynamic nuclear polarization, J. Chem. Phys. 159 (15) (2023).

[36] A. Sarkar, B. Blankenship, E. Druga, A. Pillai, R. Nirodi, S. Singh, A. Oddo, P. Reshetikhin, A. Ajoy, Rapidly enhanced spin-polarization injection in an optically pumped spin ratchet, Phys. Rev. Appl. 18 (3) (2022) 034079.

[37] K. Harkins, C. Fleckenstein, N. D'Souza, P.M. Schindler, D. Marchiori, C. Artiaco, Q. Reynard-Feytis, U. Basumallick, W. Beatrez, A. Pillai, et al., Nanoscale engineering and dynamical stabilization of mesoscopic spin textures, 2023, arXiv preprint arXiv:2310.05635.

[38] M. Mehring, J.S. Waugh, Phase transients in pulsed NMR spectrometers, Rev. Sci. Instrum. 43 (4) (1972) 649–653.

[39] A. Ajoy, X. Lv, E. Druga, K. Liu, B. Safvati, A. Morabe, M. Fenton, R. Nazaryan, S. Patel, T. Sjolander, et al., Wide dynamic range magnetic field cycler: Harnessing quantum control at low and high fields, Rev. Sci. Instrum. 90 (1) (2019).

[40] E. Fukushima, Experimental Pulse NMR: A Nuts and Bolts Approach, CRC Press, 2018.

[41] W. Beatrez, O. Janes, A. Akkiraju, A. Pillai, A. Oddo, P. Reshetikhin, E. Druga, M. McAllister, M. Elo, B. Gilbert, et al., Floquet prethermalization with lifetime exceeding 90 s in a bulk hyperpolarized solid, Phys. Rev. Lett. 127 (17) (2021) 170603.

[42] O. Sahin, E. de Leon Sanchez, S. Conti, A. Akkiraju, P. Reshetikhin, E. Druga, A. Aggarwal, B. Gilbert, S. Bhave, A. Ajoy, High field magnetometry with hyperpolarized nuclear spins, Nat. Commun. 13 (1) (2022) 5486.

[43] O. Sahin, H.A. Asadi, P. Schindler, A. Pillai, E. Sanchez, M. Markham, M. Elo, M. McAllister, E. Druga, C. Fleckenstein, et al., Continuously tracked, stable, large excursion trajectories of dipolar coupled nuclear spins, 2022, arXiv preprint arXiv:2206.14945.

[44] M.D. Dryden, R. Fobel, C. Fobel, A.R. Wheeler, Upon the shoulders of giants: Open-source hardware and software in analytical chemistry, Anal. Chem. 89 (8) (2017) 4330–4338.

[45] I. Kaminker, R. Barnes, S. Han, Arbitrary waveform modulated pulse EPR at 200 GHz, J. Magn. Reson. 279 (2017) 81–90.

[46] K. Takeda, OPENCORE NMR: Open-source core modules for implementing an integrated FPGA-based NMR spectrometer, J. Magn. Reson. 192 (2) (2008) 218–229.

[47] K. Takeda, A highly integrated FPGA-based nuclear magnetic resonance spectrometer, Rev. Sci. Instrum. 78 (3) (2007).

[48] D. Ariando, C. Chen, M. Greer, S. Mandal, An autonomous, highly portable NMR spectrometer based on a low-cost system-on-chip (SoC), J. Magn. Reson. 299 (2019) 74–92.

[49] H.-Y. Chen, Y. Kim, P. Nath, C. Hilty, An ultra-low cost NMR device with arbitrary pulse programming, J. Magn. Reson. 255 (2015) 100–105.

[50] M.C. Tayler, S. Bodenstedt, NMRduino: A modular, open-source, low-field magnetic resonance platform, J. Magn. Reson. 362 (2024) 107665.

[51] B. Andrews, M. Lai, Z. Wang, N. Kato, M. Tayler, E. Druga, A. Ajoy, High-sensitivity multichannel zero-to-ultralow field NMR with atomic magnetometer arrays, 2024, arXiv preprint arXiv:2407.00929.

[52] H. Esmaeilizadshali, S. Lehmkuhl, J. Korvink, M. Jouda, Localized shims enable low-field simultaneous multinuclear NMR spectroscopy, Anal. Chem. 96 (43) (2024) 17201–17208.

[53] D.V. Else, C. Monroe, C. Nayak, N.Y. Yao, Discrete time crystals, Annu. Rev. Condens. Matter Phys. 11 (1) (2020) 467–499.

[54] J. Zhang, P.W. Hess, A. Kyprianidis, P. Becker, A. Lee, J. Smith, G. Pagano, I.-D. Potirniche, A.C. Potter, A. Vishwanath, et al., Observation of a discrete time crystal, Nat. 543 (7644) (2017) 217–220.

[55] X. Mi, M. Ippoliti, C. Quintana, A. Greene, Z. Chen, J. Gross, F. Arute, K. Arya, J. Atalaya, R. Babbush, et al., Time-crystalline eigenstate order on a quantum processor, Nat. 601 (7894) (2022) 531–536.

[56] W. Beatrez, C. Fleckenstein, A. Pillai, E. de Leon Sanchez, A. Akkiraju, J. Diaz Alcala, S. Conti, P. Reshetikhin, E. Druga, M. Bukov, et al., Critical prethermal discrete time crystal created by two-frequency driving, Nat. Phys. 19 (3) (2023) 407–413.

[57] L.J.I. Moon, P.M. Schindler, R.J. Smith, E. Druga, Z.-R. Zhang, M. Bukov, A. Ajoy, Discrete time crystal sensing, 2024, arXiv preprint arXiv:2410.05625.

[58] L.J.I. Moon, P.M. Schindler, Y. Sun, E. Druga, J. Knolle, R. Moessner, H. Zhao, M. Bukov, A. Ajoy, Experimental observation of a time rondeau crystal: Temporal disorder in spatiotemporal order, 2024, arXiv preprint arXiv:2404.05620.

[59] W.-K. Rhim, D. Burum, D. Elleman, Multiple-pulse spin locking in dipolar solids, Phys. Rev. Lett. 37 (26) (1976) 1764.

[60] D. Li, A. Dementyev, Y. Dong, R. Ramos, S. Barrett, Generating unexpected spin echoes in dipolar solids with $\pi$ pulses, Phys. Rev. Lett. 98 (19) (2007) 190401.

[61] K.A. Harkins, C. Selco, C. Bengs, D. Marchiori, L.J.I. Moon, Z.-R. Zhang, A. Yang, A. Singh, E. Druga, Y.-Q. Song, et al., Anomalously extended floquet prethermal lifetimes and applications to long-time quantum sensing, 2024, arXiv preprint arXiv:2410.09028.

[62] M. Sarovar, H.-S. Goan, T. Spiller, G. Milburn, High-fidelity measurement and quantum feedback control in circuit QED, Phys. Rev. At. Mol. Opt. Phys. 72 (6) (2005) 062327.

[63] R. Vijay, C. Macklin, D. Slichter, S. Weber, K. Murch, R. Naik, A.N. Korotkov, I. Siddiqi, Stabilizing rabi oscillations in a superconducting qubit using quantum feedback, Nat. 490 (7418) (2012) 77–80.

[64] S. Mavadia, V. Frey, J. Sastrawan, S. Dona, M.J. Biercuk, Prediction and real-time compensation of qubit decoherence via machine learning, Nat. Commun. 8 (1) (2017) 14106.